Polymer Testing 131 (2024) 108325

Contents lists available at ScienceDirect

Polymer Testing

journal homepage: www.elsevier.com/locate/polytest

Constrained amorphous interphase in plasticized poly(lactic acid): Composition and tensile elastic modulus estimation

Giovanna Molinari [a,b], Laura Aliotta [a,c], Mauro Gemmi [b], Andrea Lazzeri [a,c], Maria Cristina Righetti [d,*]

[a] Department of Civil and Industrial Engineering, University of Pisa, 56122, Pisa, Italy
[b] Center for Materials Interfaces, Istituto Italiano di Tecnologia, 56025, Pontedera, Italy
[c] National Interuniversity Consortium of Materials Science and Technology (INSTM), 50121, Florence, Italy
[d] CNR-IPCF, National Research Council – Institute for Chemical and Physical Processes, 56124, Pisa, Italy

ARTICLE INFO

Keywords:
Poly(lactic acid)
Plasticizer
Crystallinity
Rigid amorphous fraction
Mobile amorphous fraction
Tensile elastic modulus

ABSTRACT

The study investigates the distribution of the plasticizers acetyl triethyl citrate (ATEC) and acetyl tributyl citrate (ATBC) in the mobile amorphous (MAF) and rigid amorphous (RAF) fractions of semi-crystalline plasticized poly (lactic acid) (PLA) containing 5 wt% of plasticizer. During crystallization, the ATEC and ATBC concentration in the MAF increases from 5 to about 8 wt%. At the end of crystallization, the plasticizers concentration in the RAF is lower than that in the MAF. The progressive decrease of the ATEC and ATBC concentration in the RAF region could be linked to the growth of subsidiary lamellae in more restricted amorphous areas. The study also introduces an estimation of the tensile elastic modulus of the RAF (E_{RAF}) in semi-crystalline pure and plasticized PLA containing α-crystals. The mechanical model with crystalline lamellae perpendicular to the stress direction turned out to be the most appropriate arrangement to represent the morphological organization in PLA samples prepared by injection-moulding processing at high pressure. The mathematical procedure led to a crystal elastic modulus (E_C) of the α-phase in excellent agreement with the theoretical value reported in the literature ($E_C = 14$ GPa), and to an E_{RAF} value around 5.5 GPa, for both pure and plasticized PLA, thus suggesting that both ATEC and ATBC do not exert plasticizing action on the RAF.

1. Introduction

Nowadays, poly (lactic acid) (PLA) is certainly the most studied bio-based and biodegradable polymer. As lactic acid exists in L- and D-enantiomers, PLAs with different chirality can be synthesized. Homopolymers poly (L-lactic acid) (PLLA) and poly (D-lactic acid) (PDLA) contain exclusively L-lactic acid and D-lactic acid units, respectively, whereas PLA copolymers are mixtures of L- and D-units. Commercial PLA grades are generally copolymers of PLLA containing a small percentage of D-units, because L-enantiomer is the isomer mainly derived from renewable sources [1,2]. The distribution of the L- and D-sequences strongly influences the crystallization ability of the PLA copolymers. Crystallinity, crystallization rate, and melting temperature decrease with increasing the D-units percentage. Thus, PLA copolymers containing more than 10–15 % of randomly distributed D-units are totally amorphous [3].

Different crystalline structures develop in PLLA as a function of the crystallization conditions [4]. The most stable crystal form (α) grows at temperatures higher than 120 °C during melt and cold crystallizations under normal conditions in absence of stretching. The α-form is characterized by a left-handed 10_3 helical conformation packed in an orthorhombic unit cell. At temperatures lower than 100 °C a slightly more disordered crystal form with looser packing, the α′-form, develops, whereas a mixture of α′- and α-crystals grows between 100 and 120 °C. Around 150–160 °C, the disordered α′-form irreversibly transforms into the more stable α-form upon heating at rates slower than 30 K/s [5]. Arguments on the occurring of this transition via melting/-recrystallization or solid-solid transition can be found in the literature [5–7]. By increasing the D-unit amount, the temperatures that characterize the α′- and the α-regions shift to lower temperatures [8–10]. Thus, for a D-unit content of about 2 %, α′-crystals grow exclusively below 90 °C and α-crystals above 110 °C [9,10].

The good thermal properties (glass transition temperature around 60 °C and melting temperature in the range 160–170 °C), together with

* Corresponding author.
E-mail address: cristina.righetti@pi.ipcf.cnr.it (M.C. Righetti).

https://doi.org/10.1016/j.polymertesting.2024.108325
Received 30 October 2023; Received in revised form 11 December 2023; Accepted 1 January 2024
Available online 6 January 2024

valuable mechanical properties (tensile elastic modulus of about 3–4 GPa and tensile strength at break in the range 50–60 MPa) make commercial PLA grades competitive with common petroleum-based polymers [11–13]. A limiting feature of PLA is its considerable brittleness, which hinders the utilization in applications which require toughness. To improve the PLA mechanical properties under this perspective, different methods have been utilized, as for example drawing and biaxial orientation [14], blending with a polymer with lower T_g, as poly (caprolactone) (PCL), poly (butylene adipate-*co*-terephthalate (PBAT), poly (butylene succinate) (PBS) or poly (butylene succinate-*co*-adipate) (PBSA) [15–18], and plasticization, which is a very fast and practical procedure [11–13].

The addition of a plasticizer generally favours the processability of a polymer and increases its ductility and flexibility. The intermolecular interactions between the polymer chains are broken and new interactions can be established between the polymer and the plasticizer. The presence of plasticizer molecules reduces the intermolecular interactions density between the polymer chains as well as the size of the cooperativity region at the glass transition temperature, so that the macromolecular mobility increases and T_g decreases [19]. Moreover, additional free volume is introduced due to the motions of the portions of the plasticizer molecules that do not interact with the macromolecular chains [20]. Non-toxic and biodegradable ("green") plasticizers of PLA are: lactide monomers, lactic acid oligomers, oligomeric or polymeric poly (eythylene glycol) (PEG) and poly (propylene glycol) (PPG) [11–13], and citrate esters (triethyl citrate (TEC), tributyl citrate (TBC), acetyl triethyl citrate (ATEC) and acetyl tributyl citrate (ATBC)), which are miscible with PLA up to about 25 wt% [21–28].

In general, during crystallization of plasticized polymers, the non-crystallizable additive diffuses away from the crystal growth front and its concentration increases in the amorphous phase. This can produce an increase in the overall crystallization rate, as also found for the PLA/ATBC system [10,29]. Acceleration of the crystal growth rate can be sometimes observed also with the progress of crystallization at high crystallization times, as for example for PLA/PEG and PLA/PPG systems, suggesting plasticizer accumulation in front of the growing spherulites [30,31]. As regards citrate esters, in a study on PLA/TEC mixtures, a constant crystal growth rate was measured, which proved that during crystallization, TEC moves from the crystalline regions into the amorphous phase without segregating at the amorphous/crystal boundary [27]. The difference between ATEC and TEC is that a hydroxyl group in TEC is replaced by an acetate group in ATEC, which suggests stronger PLA/TEC interactions with respect to PLA/ATEC, and therefore possible slower TEC mobility in comparison with ATEC mobility in the PLA matrix. As regards ATBC, it is characterized also by higher steric dimensions, which in turn could slow down its mobility in the polymer. Thus, the migration behaviour of ATEC and ATBC could be substantially different from that of TEC.

An estimation of the rise in the plasticizer concentration in the amorphous phase after crystallization can be useful for a more accurate interpretation of macroscopic properties, as for example, mechanical properties. A detailed analysis of the evolution of the plasticizer concentration must take into account also the interphase at the amorphous/crystal boundary. It consists of a nanometric amorphous layer with mobility reduced with respect to the amorphous regions far from the crystals, due to its coupling with the crystals by covalent bonds [32–34]. This constrained or rigid amorphous fraction (RAF) vitrifies/devitrifies at temperatures higher than T_g, which is defined as the glass transition temperature of the mobile amorphous fraction (MAF), *i.e.* the amorphous region far from the crystals.

In the present study, two plasticizers of PLA with similar chemical structure but different steric hindrance have been considered, namely ATEC and ATBC, and the analysis of the plasticizers distribution in the MAF and RAF regions of PLA/ATEC and PLA/ATBC mixtures has been performed. A low ATEC and ATBC amount was utilized (5 wt%), to avoid plasticizer loss during processing, which is proportional to its concentration [21] and possible migration [35].

It is known that the mechanical properties of semi-crystalline polymers depend on microstructure and phase composition. The RAF also contributes with its peculiarity to the mechanical response. Several experimental and theoretical investigations have demonstrated that the elastic modulus of the RAF is higher than that of the MAF, thus attesting that the constrained interphase plays an important role on the stress transfer between the crystalline and mobile amorphous phases [36–39]. A mechanical model that was proven useful for predicting the tensile elastic modulus of semi-crystalline polymers is the Takayanagi model [40], a combination of series and parallel elements that can describe the different deformations that the various phases undergo under stress. The original two-phase Takayanagi model does not consider the amorphous/crystal interphase, which displays organization and mobility significantly different from the amorphous phase far from the crystals. For this reason, the model has been recently modified and transformed into a three-phase model, for a better and more accurate interpretation of the tensile elastic modulus of semi-crystalline polymers as a function of the correct phase composition [41,42]. By means of this procedure, the elastic modulus of the RAF in PLLA and some poly (3-hydroxy-*co*-3-hydroxyvalerate) copolymers was estimated, and the moduli of the crystalline (E_C), mobile amorphous (E_{MAF}) and rigid amorphous (E_{RAF}) fractions turned out to be quantitatively in the order $E_{MAF} < E_{RAF} < E_C$ [41,42]. The same analysis is here applied to PLA/ATEC and PLA/ATBC mixtures. The aim is the estimation of the RAF elastic modulus in plasticized PLA, for an accurate prediction of the mechanical properties of these materials in comparison with pure PLA. The knowledge of the properties of the different fractions, also by means of theoretical methods, can support the design of materials with targeted and tailored properties.

2. Materials and methods

2.1. Materials

Commercial PLA Ingeo 4032D, containing 1.4 ± 0.2 % of D-isomer [43] [melt flow index (MFR): 7 g/10 min (210 °C, 2.16 kg)], was purchased from NatureWorks LLC. Acetyl tributyl citrate (ATBC) was purchased from Tecnosintesi S. p.A (Bergamo, Italy). It is a colourless and odourless liquid with a density of 1.05 g/cm^3 at room temperature, and a molecular weight of 402.5 g/mol [21]. Acetyl triethyl citrate (ATEC), was purchased from TCI Europe N.V. It is a colourless liquid with a density of 1.14 g/cm^3 at 20 °C and a molecular weight of 318.3 g/mol [21].

2.2. Sample preparation

Pure PLA 4032D and plasticized PLA 4032D samples (with composition reported in Table 1) were processed in a Comac EBC 25 H T (L/D = 44) (Comac, Cerro Maggiore, Italy) semi-industrial twin screw extruder to obtain the pellets for the subsequent injection moulding processing. The present study investigates in detail the mixtures PLA_ATEC_5 and PLA_ATBC_5 in comparison with pure PLA. Mixtures with higher plasticizers amount were prepared and analysed to assist the data interpretation and discussion.

Table 1
Samples composition in weight fractions (*wt*).

Sample	PLA [*wt*]	ATEC [*wt*]	ATBC [*wt*]
PLA	1.00	–	–
PLA_ATEC_5	0.95	0.05	
PLA_ATEC_7	0.93	0.07	–
PLA_ATEC_9	0.91	0.09	–
PLA_ATBC_5	0.95	–	0.05
PLA_ATBC_7	0.93	–	0.07
PLA_ATBC_9	0.91	–	0.09

Before extrusion, the as received PLA granules were dried in a Piovan DP 615 dryer (Venezia, Italy) at 60 °C for 24 h. PLA pellets were introduced into the main extruder feeder, while the plasticizers were added using a peristaltic pump (Verderflex - Vantage3000) suitably calibrated to guarantee a constant flow rate and the fixed plasticizer concentration. The temperature profile adopted during the extrusion in the zones from 1 to 11 was 165/175/180/180/185/185/185/185/185/185/185 °C, with the die zone at 170 °C. The screw rate was 350 rpm, and the total mass flow rate was 15 kg/h. The extruded strands were cooled in a water bath at room temperature and reduced in pellets by an automatic knife cutter. Finally, all pellets were dried in the above mentioned Piovan dryer at 40 °C for 12 h.

The extruded pellets were injection-moulded in a Megatech H10/18 injection-moulding machine (Tecnica Duebi s. r.l., Fabriano, Italy) to obtain ISO 527-1 A dog-bone specimens (width: 10 mm, thickness: 4 mm, length: 80 mm). Amorphous and semi-crystalline specimens were prepared by varying the moulding temperature (T_{mould}) and moulding time (t_{mould}). The operative parameters of the injection-moulding process are reported in Table 2. The temperature of the feeder/injection zone was 185 °C for pure PLA and 180 °C for plasticized PLA. After processing, all the specimens were quickly cooled to T_{room} in less than 1 min by means of cold air. The injection-moulded samples were stored in a dry keeper (Sanplantec Corp., Osaka, Japan) at T_{room} in a controlled atmosphere (50 % relative humidity) and analysed 3 days after preparation.

Thermogravimetric measurements were performed to confirm the plasticizers concentration in the PLA_ATEC_5 and PLA_ATBC_5 mixtures after processing. The results and discussion are reported in the Supplementary Data.

2.3. Thermal characterization by differential scanning calorimetry (DSC) and temperature-modulated differential scanning calorimetry (TMDSC)

DSC and TMDSC measurements were performed with a PerkinElmer Calorimeter DSC 8500 (Waltham, Massachusetts, USA) equipped with an IntraCooler III as refrigerating system. The instrument was calibrated in temperature with high-purity standard materials (indium, naphthalene, and cyclohexane) at zero heating rate according to the procedure for conventional DSC [44]. Enthalpy calibration was performed with indium. To minimize the instrumental thermal lag, the sample mass was lower than 10 mg. Small pieces of the injection moulded specimens were obtained by using a wire cutter. Portions from the external surfaces and the more inner regions were analysed. Non-hermetic aluminium pans were utilized. To gain precise specific heat capacity data from the heat flow rate signal, each scan was accompanied by an empty pan run (blank run). The mass of the blank and sample aluminium pan matched within 0.02 mg. Dry nitrogen (99.999 % pure) was used as purge gas at a rate of 20 mL/min. The temperature upon heating was corrected for the thermal lag, averaged on different standard materials. This lag was 0.05 min, which for the heating rates of 2 and 10 K/min, corresponds to a temperature correction of −0.1, and −0.5 K, respectively.

The injection-moulded pure and plasticized PLA samples were analysed by: (*i*) conventional DSC from 20 to 190 °C (to 185 °C when plasticizers were present) at the heating rate of 10 K/min to obtain apparent specific heat capacity ($c_{p,app}$) curves; (*ii*) TMDSC, with a saw-tooth modulation temperature program, at the average heating rate of 2 K/min, with a temperature amplitude (A_T) of 0.5 K and a modulation period (p) of 120 s, to obtain average specific heat capacity ($c_{p,ave}$) curves and reversing specific heat capacity ($c_{p,rev}$) curves. According to the mathematical treatment of TMDSC data, the modulated temperature and heat flow rate curves can be approximated to discrete Fourier series and separated into average and periodic components [45,46]. The average components are equivalent to the conventional linear program of the temperature and the corresponding conventional heat flow rate signal, from which the $c_{p,ave}$ curve can be derived. Conversely, from the periodic component, the $c_{p,rev}$ curve is calculated according to Eq. (1):

$$c_{p,rev}(\omega, T) = \frac{A_{HF}(T)}{A_T(T)} \frac{K(\omega)}{m\omega} \quad (1)$$

where A_{HF} and A_T are the amplitudes of the first harmonic of the modulated heat flow rate and temperature, respectively, ω is the fundamental frequency of temperature modulation ($\omega = 2\pi/p$), m is the mass of the sample, and $K(\omega)$ is the frequency-dependent calibration factor. The average $K(\omega)$ value, determined by calibration with sapphire, was 1.00 ± 0.02 for $p = 120$ s.

The specific heat capacities of pure ATEC and ATBC were determined as $c_{p,rev}$ by means of TMDSC scans in the temperature range 20–60 °C (average heating rate: 2 K/min, $A_T = 0.5$ K and $p = 120$ s) by utilizing hermetic aluminium pans, to avoid evaporations of the plasticizers.

2.4. Tensile characterization

Uniaxial tensile tests were carried out on the injection-moulded ISO 527-1 A dog-bone specimens using a MTS Criterion model 43 universal testing machine (MTS Systems Corporation, Eden Prairie, MN, USA) equipped with a 10 kN load cell and interfaced with computer running MTS Elite Software. At least ten specimens for each material composition were tested at a constant crosshead speed of 10 mm/min and the average values are reported.

2.5. X-ray diffraction (XRD) analysis

XRD data were acquired in transmission/Debye-Scherrer geometry using a STOE Stadi P diffractometer equipped with Cu tube monochromated on the Cu-Kα1 radiation (λ = 1.5406 Å) by a Ge (1 1 1), a Johansson monochromator and a MYTHEN2 1 K detector from Dectris. The line focused Cu X-ray tube was operated at 40 kV and 40 mA. For the XRD analysis, small portions of the dog-bone specimens were cut out from the central area by using a jigsaw (width: approx. 5 mm, length approx. 5 mm, thickness: 4 mm). These specimens contained both surface and internal sections of the dog-bone specimens. Data were acquired in the 2θ range 2–60° (maximum resolution ca. 1.5 Å) with a step of 0.03° between consecutive points. A scan without samples was performed and subtracted from each scan, to avoid the air and incoherent scattering contributions. The X-ray crystalline fractions (X_C^{XRD}) were calculated as the ratio between the areas of the crystalline peaks and the total area of the background corrected diffraction profiles. The lattice constants were calculated from the positions of the most intense XRD peaks ascribable to the PLA α-form.

Table 2
Operating conditions of the injection-moulding process of PLA and plasticized PLA.

Amorphous samples	Conditions
PLA PLA_ATEC_5 PLA_ATEC_7 PLA_ATEC_9 PLA_ATBC_5 PLA_ATBC_7 PLA_ATBC_9	temperature of the feeder/injection zone: 180/185 °C injection holding time: 10 s injection pressure: 180 bar moulding temperature (T_{mould}): 60 °C moulding time (t_{mould}): <1 min
Semi-crystalline samples	**Conditions**
PLA PLA_ATEC_5 PLA_ATBC_5	temperature of the feeder/injection zone: 180/185 °C injection holding time: 10 s injection pressure: 180 bar moulding temperature (T_{mould}): 120 °C moulding time (t_{mould}): 6 min ≤ t_{mould} ≤ 20 min

3. Results and discussion

3.1. Thermal characterization of amorphous and semi-crystalline pure and plasticized PLA samples

Fig. 1 shows the $c_{p,rev}$, $c_{p,ave}$ and $c_{p,app}$ curves of the amorphous PLA, PLA_ATEC_5 and PLA_ATBC_5 samples, prepared by injection-moulding, together with the corresponding thermodynamic solid and liquid specific heat capacities. For pure PLA, the solid and liquid specific heat capacities ($c_{ps,PLA}$ and $c_{pl,PLA}$) were determined by averaging several $c_{p,rev}$ curves in the glassy and liquid regions, respectively. It can be noted that in the cold crystallization region $c_{p,rev}$ displays irregular oscillations. These undulations are artefacts connected to the fast release of crystallization latent heat [47]. In the present study, the $c_{p,rev}$ curves were considered only in the glassy and liquid states for the determination of the thermodynamic specific heat capacities. The derived $c_{ps,PLA}$ and $c_{pl,PLA}$ expressions are in very good agreement with literature data [48]: $c_{ps,PLA} = 1.16 + 0.0033 \cdot T$ (°C) and $c_{pl,PLA} = 1.80 + 0.0012 \cdot T$ (°C), with $c_{ps,PLA}$ and $c_{pl,PLA}$ in J/(g K). The measured specific heat capacities of ATEC and ATBC in the temperature range 20–60 °C (see Fig. S2 in the Supplementary Data), were $c_{p,ATEC} = 1.68 + 0.0014 \cdot T$ (°C) in J/(g K) and $c_{p,ATBC} = 1.71 + 0.0024 \cdot T$ (°C) in J/(g K), the latter one in excellent agreement with literature data [49]. By assuming simple additivity, the solid and liquid specific heat capacity of the plasticized PLA samples (c_{ps,PLA_plast} and c_{pl,PLA_plast}) in the temperature range 20–60 °C were calculated as: $c_{ps,PLA\_plast} = wt_{PLA}\, c_{ps,PLA} + wt_{plast}\, c_{p,plast}$ and $c_{pl,PLA\_plast} = wt_{PLA}\, c_{pl,PLA} + wt_{plast}\, c_{p,plast}$, where $c_{p,plast}$ is the specific heat capacity of the plasticizer and wt_{PLA} and wt_{plast} the PLA and plasticizer weight fractions.

Fig. 1 shows that the specific heat capacity increments at T_g for pure and plasticized PLA match with the difference between the corresponding thermodynamic liquid and solid specific heat capacities, which confirms that these samples are completely amorphous. This finding also proves that the addition of the plasticizers ATEC and ATBC to PLA does not lead to the development of strong specific interactions between the two mixture components, due to the absence of an excess specific heat capacity contribution to c_{ps,PLA_plast} and c_{pl,PLA_plast} [50]. By considering that the chemical structure of ATEC and ATBC largely consists of COO and CH_3 groups, it can be supposed that the same interactions active in pure PLA are established also between PLA and the plasticizers.

The $c_{p,app}$ curves shown in Fig. 1 display the glass transition overlapped by a small enthalpy recovery peak, as a consequence of the structural relaxation that occurred during the storage at T_{room} after preparation. The glass transition temperature (T_g) values of the amorphous pure and plasticized PLA samples, determined at half of the heat capacity increment of the $c_{p,rev}$ curves, are listed in Table 3. Fig. 1 and Table 3 show that the addition of 5 wt% of ATEC and ATBC leads to a decrease in T_g of about 10 K, in agreement with previous studies [19,23,25].

Both pure and plasticized PLA undergo cold crystallization upon heating. Cold crystallization occurs at lower temperatures when the samples are heated at 2 K/min. From Fig. 1 it appears clear that plasticization favours cold crystallization, which occurs at slightly lower temperatures with respect to pure PLA, as also previously reported in the literature [10,23,25]. Cold crystallization that arises upon heating at 2 K/min leads to the growth of α′-crystals, because it occurs below 100 and 90 °C for pure and plasticized PLA, respectively [4,9,10] as also attested by the typical exothermic peak in the $c_{p,ave}$ curves at about 150 °C, due to the reorganization/recrystallization of the disordered α′-crystals into the more ordered α-form [5–7]. During cold crystallization at 10 K/min, a mixture of α′- and α-crystals grows in pure and plasticized PLA, because this process occurs between 90 and 120 °C [4,9,10]. At 10 K/min the exotherm before final melting is barely detected in the $c_{p,app}$ curves, due to the lower percentage of α′-crystals, in perfect agreement with a previous study [51].

Fig. 2 shows the $c_{p,rev}$, $c_{p,ave}$ and $c_{p,app}$ curves of the semi-crystalline PLA, PLA_ATEC_5 and PLA_ATBC_5 samples after complete crystallization (t_{mould} = 20 min) at T_{mould} = 120 °C (Fig. S3 in the Supplemental Data displays the $c_{p,rev}$, $c_{p,ave}$ and $c_{p,app}$ curves after lower t_{mould}s). In Fig. 2, the $c_{p,app}$ and $c_{p,ave}$ curves appear substantially different from the $c_{p,rev}$ curves in the region slightly above T_g. Reversing heat capacity originates from the amplitude of the endothermic and exothermic events that follow the temperature modulation, whereas $c_{p,app}$ and $c_{p,ave}$ algebraically account for the latent heats released or absorbed during the heating scan [52], with the result that the glass transition can be partially or completely masked in the $c_{p,app}$ and $c_{p,ave}$ curves if irreversible endothermic or exothermic events occurs simultaneously. Conversely, $c_{p,rev}$ can resolve the glass transition in the presence of concurrent irreversible processes [53]. Thus, the $c_{p,rev}$ curve reproduces the true glass transition event, whereas the difference between $c_{p,app}$ or $c_{p,app}$ and $c_{p,rev}$ has to be associated with processes that irreversibly absorb or release enthalpy. The different shape of the $c_{p,app}$ and $c_{p,rev}$ curves in the region slightly above T_g is not ascribable to cold crystallization, which occurs at higher temperature (see Fig. 1). Conversely, it is the consequence of the moulding process under pressure [54]. In the presence of physical constraints due to crystals, a pressure-densified glass can relax to a less dense glass with lower enthalpy when chain mobility is sufficiently high, as it can occur above T_g [42,54].

The T_g values, determined from the $c_{p,rev}$ curves for all the PLA and plasticized PLA samples after different moulding times at T_{mould} = 120 °C, are listed in Table 3. The glass transition temperature of pure

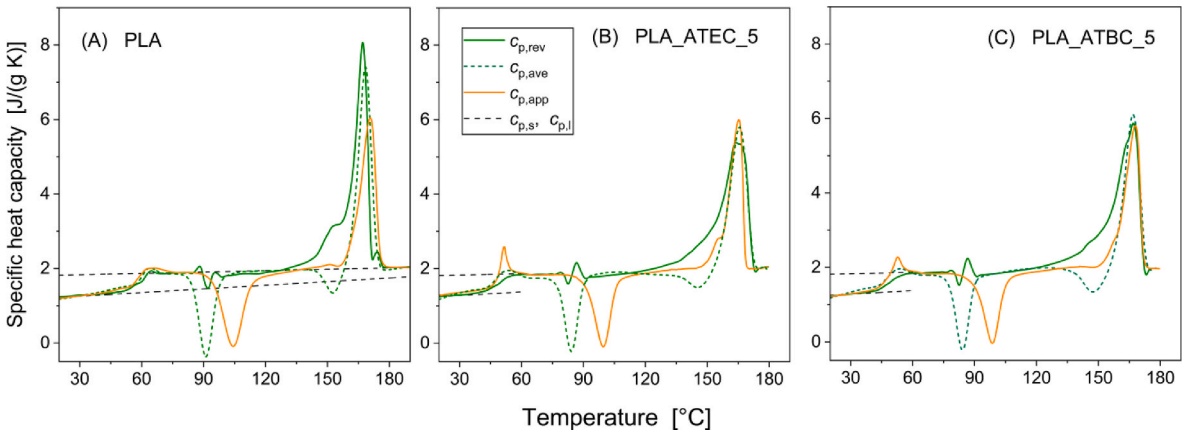

Fig. 1. Reversing specific heat capacity ($c_{p,rev}$, solid green line), average specific heat capacity ($c_{p,ave}$, dashed green line) at the average heating rate of 2 K/min (p = 120 s) and apparent specific heat capacity ($c_{p,app}$, solid orange line) at the heating rate of 10 K/min for amorphous (A) PLA, (B) PLA_ATEC_5 and (C) PLA_ATBC_5. The black dotted lines are the respective thermodynamic solid and liquid specific heat capacities, determined as described in the text.

Table 3
Glass transition temperatures (T_g); mobile amorphous weight fraction of PLA ($w_{MAF,PLA}$); crystalline weigh fraction of PLA ($w_{C,PLA}$); crystalline fraction of PLA by XRD ($X^{XRD}_{C,PLA}$); rigid amorphous weight fraction of PLA ($w_{RAF,PLA}$); experimental elastic modulus (E); tensile strength at break (TS), elongation at break at T_{room} for pure PLA, PLA_ATEC_5 and PLA_ATBC_5 (amorphous and after crystallization at $T_{mould} = 120$ °C for different moulding times). For the PLA_ATEC_5 and PLA_ATBC_5 samples the sum ($w_{MAF,PLA}+w_{C,PLA}+w_{RAF,PLA}$) is equal to 0.95. Estimated errors from repeated measurements: ±0.5 K for T_g; ± 0.02 for $w_{MAF,PLA}$, $w_{C,PLA}$ and $X^{XRD}_{C,PLA}$; ±0.04 for $w_{RAF,PLA}$; ±0.05 GPa for E; ±1 MPa for TS; ±0.2 for the elongation at break.

Sample	T_g [°C]	$w_{MAF,PLA}$	$w_{C,PLA}$	$X^{XRD}_{C,PLA}$	$w_{RAF,PLA}$	E [GPa]	TS [MPa]	Elongation at break [%]
PLA								
amorphous	60.0	1.00	0.00	–	0.00	3.27	61	3.0
$T_{mould} = 120$ °C, $t_{mould} = 6$ min	60.0	0.73	0.16	–	0.11	3.55	58	2.0
$T_{mould} = 120$ °C, $t_{mould} = 10$ min	61.0	0.54	0.30	–	0.16	4.02	57	1.4
$T_{mould} = 120$ °C, $t_{mould} = 20$ min	61.0	0.50	0.31	0.31	0.19	4.10	57	1.4
PLA_ATEC_5								
amorphous	48.5	0.95	0.00		0.00	3.15	50	4.0
$T_{mould} = 120$ °C, $t_{mould} = 10$ min	46.5	0.69	0.19	–	0.07	3.45	43	2.9
$T_{mould} = 120$ °C, $t_{mould} = 14$ min	45.0	0.58	0.28	–	0.09	3.89	38	2.0
$T_{mould} = 120$ °C, $t_{mould} = 20$ min	44.0	0.56	0.29	0.30	0.10	3.98	37	2.0
PLA_ATBC_5								
amorphous	49.0	0.95	0.00	–	0.00	3.13	55	3.9
$T_{mould} = 120$ °C, $t_{mould} = 10$ min	47.0	0.66	0.24	–	0.05	3.87	44	2.2
$T_{mould} = 120$ °C, $t_{mould} = 14$ min	45.5	0.55	0.30	–	0.10	3.95	42	1.6
$T_{mould} = 120$ °C, $t_{mould} = 20$ min	44.5	0.50	0.31	0.31	0.14	4.01	40	1.6

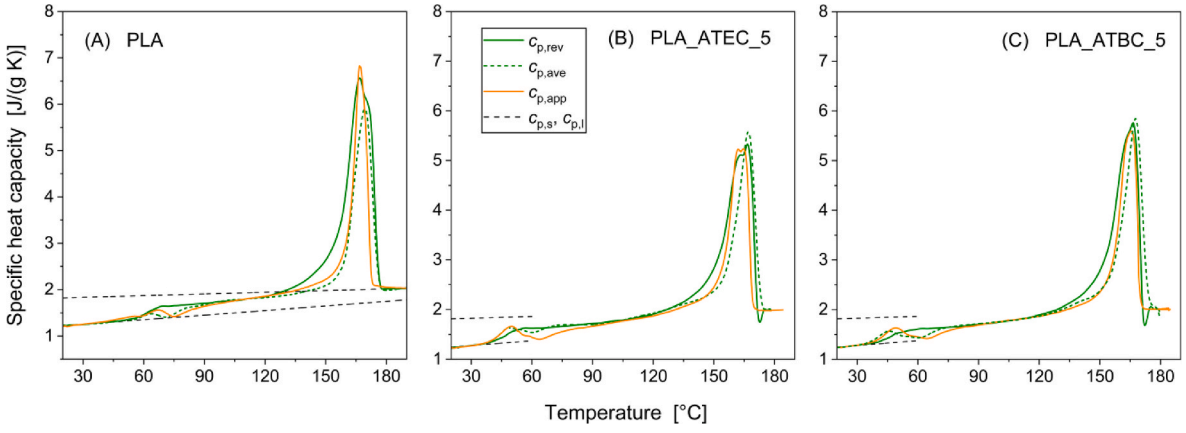

Fig. 2. Reversing specific heat capacity ($c_{p,rev}$, solid green line), average specific heat capacity ($c_{p,ave}$, dashed green line) at the average heating rate of 2 K/min (p = 120 s) and apparent specific heat capacity ($c_{p,app}$, solid orange line) at the heating rate of 10 K/min for semi-crystalline ($T_{mould} = 120$ °C, $t_{mould} = 20$ min) (A) PLA, (B) PLA_ATEC_5 and (C) PLA_ATBC_5. The black dotted lines are the respective thermodynamic solid and liquid specific heat capacities, determined as described in the text.

PLA slightly increases with the progress of crystallization, due to progressively reduced amorphous chain mobility, as a consequence of the rising constraints caused by the crystalline structures [33]. Conversely, for plasticized PLA, the T_g values decrease as t_{mould} increases. In this case, the effect of the plasticizer accumulation in the amorphous phase during the crystallization process, with consequent T_g reduction, is evidently dominant [30,31,49] with respect to the increase in the physical constraints. The T_g values of the PLA_ATEC_5 samples appear slightly lower than that of the PLA_ATBC_5 samples.

Fig. 2 and Fig. S3 display that the melting of semi-crystalline pure and plasticized PLA consists of two barely resolved peaks. At T_{mould} = 120 °C, only α-crystals grow, as also confirmed by XRD analysis (see below). Thus, the double melting behaviour can be explained as melting of the original α-crystals (although slightly perfected upon heating), followed by melting of recrystallized α-crystals [55].

The mobile amorphous weight fractions of PLA ($w_{MAF,PLA}$) in semi-crystalline pure and plasticized PLA samples after different t_{mould}s at $T_{mould} = 120$ °C were calculated at the respective T_gs as $w_{MAF,PLA} = \Delta c_p/\Delta c_{pa}$, where Δc_p is the specific heat capacity increment calculated from the $c_{p,rev}$ curves, and Δc_{pa} is the specific heat capacity increment of the completely amorphous pure PLA. For plasticized PLA, the units of Δc_p are [J/(g_{PLA_plast} K)], where g_{PLA_plast} is the weight of the PLA_ATEC_5 and PLA_ATBC_5 mixtures, whereas the units of Δc_{pa} are [J/(g_{PLA} K)], thus the calculated $w_{MAF,PLA}$ values, listed in Table 3, are the weight fractions of the PLA mobile amorphous phase in the mixtures PLA_ATEC_5 and PLA_ATBC_5.

The crystalline weight fractions of PLA ($w_{C,PLA}$) after different t_{mould}s at $T_{mould} = 120$ °C were estimated from the $c_{p,app}$ curves at 10 K/min as difference between the crystalline weight fraction disappearing during the melting process (w_{Cm}) and the crystalline weight fraction growing during the cold crystallization process (w_{Cc}), which is present only for the lowest t_{mould} investigated (see Fig. S3 and Table S1). *i.e.* $w_{C,PLA} = w_{Cm} - w_{Cc}$. In detail, w_{Cm} was calculated dividing the experimental enthalpy of melting (Δh_m) by the enthalpy of melting of 100 % crystalline α-crystals at the average melting peak temperature of 167 °C (Δh_m° = 139 J/g) [56], whereas w_{Cc}, which is connected to the crystallization of a mixture of α′- and α-crystals, was obtained dividing the enthalpy of cold crystallization (Δh_c) by the average enthalpy of fusion

of 100 % crystalline α′- and α-crystals at the average crystallization temperature of 100 °C (Δh_m° = 96 J/g) [56]. (The occurring of exothermic α'- α transformation upon heating for the lowest t_{mould} investigated was not considered, due to the low measured Δh_c values.) Table S1 in the Supplementary Material lists the average Δh_c and Δh_m values obtained from several repeated measurements on portions of the injection-moulded specimens near and far from the external surfaces. For plasticized PLA, the units of Δh_m and Δh_c are [J/g_{PLA_plast}], whereas those of Δh_m° are [J/g_{PLA}], thus the calculated $w_{C,PLA}$ values, listed in Table 3, are the weight fractions of the crystal phase in the PLA_ATEC_5 and PLA_ATBC_5 mixtures.

For comparison, the crystalline weight fractions of the completely crystallized PLA, PLA_ATEC_5 and PLA_ATBC_5 samples were also determined by XRD analysis ($X_{C,PLA}^{XRD}$) (see section below and Table 3). The very good agreement between the crystallinities determined by means of two different techniques confirms the accuracy of the Δh_m° values utilized for the calculation of $w_{C,PLA}$.

From the crystalline and mobile amorphous fractions, the rigid amorphous weight fraction of PLA ($w_{RAF,PLA}$) was determined by difference: as $w_{RAF,PLA}$=1-$w_{C,PLA}$-$w_{MAF,PLA}$ for pure PLA, whereas as $w_{RAF,PLA}$=0.95-$w_{C,PLA}$-$w_{MAF,PLA}$ for plasticized PLA.

Inspection of Table 3 discloses that PLA plasticization with ATEC and ATBC does not significantly alter the phase composition in the semi-crystalline samples. The only relevant point is that RAF appears slightly lower in the plasticized PLA samples, especially for the PLA_ATEC_5 mixture, which displays simultaneously a slightly higher MAF value. Higher mobility can be experienced also by amorphous portions quite close to the crystals, which could result in a decrease of the RAF thickness and an extension of the MAF region. This confirms that the nanostructure of the amorphous phase strongly depends on the polymer/plasticizer interactions [57]. The ratio $w_{RAF,PLA}/w_{C,PLA}$ is in perfect agreement with previous studies on pure PLLA and PLA/ATBC mixtures [33,49].

3.2. XRD analysis of semi-crystalline pure and plasticized PLA samples

Fig. 3 shows the XRD patterns at T_{room} of pure PLA, PLA_ATEC_5 and PLA_ATBC_5 after crystallization at T_{mould} = 120 °C for t_{mould} = 20 min. All patterns exhibit the profile of the α-phase, easily identified by the position of the most intense (110/200) and (203/113) peaks at the 2θ scattering angles of 16.6° and 19.0° and by the (103/004), (011) and (211) peaks at 12.5°, 14.8° and 22.3°, as well as for several other less intense reflections at higher angles [4,56].

From the position of the most intense peaks, the average crystallographic parameters were derived for the orthorhombic cell of PLA α-phase. The interplanar distances (d_{hkl}) were calculated according to the Bragg's law ($n\lambda = 2d_{hkl}\sin\theta$), and used to obtain the dimensions of the crystalline PLA cell through the equations [58]:

$$(d_{hkl})^{-2} = (h/a)^2 + (k/b)^2 + (l/c)^2 \quad (2)$$

Table 4 lists the calculated unit cell dimensions and the estimated cell volume. From these data, by assuming that the crystalline unit houses two helices with ten units in three turns [59], a crystalline density (ρ_C) of about 1.285 g/cm^3 was calculated for the crystalline α-phase of the PLA here utilized. This density value is very close to ρ_C values found in the literature [60,61]. The crystal fractions of completely crystallized PLA, PLA_ATEC_5 and PLA_ATBC_5 samples, calculated from the XRD profiles ($X_{C,PLA}^{XRD}$), are listed in Table 3 and already discussed in the previous section.

3.3. Quantification of the ATEC and ATBC concentration in the MAF and RAF regions of semi-crystalline plasticized PLA samples

An estimation of the actual ATEC and ATBC concentration in the MAF of the semi-crystalline PLA_ATEC_5 and PLA_ATBC_5 samples was performed from interpolation of the T_g vs. plasticizer content curves (see Fig. S4 in the Supplementary Data). The T_g values of amorphous PLA_ATEC and PLA_ATBC mixtures with increasing plasticizer concentration are listed in Table 5, together with mechanical properties data.

As expected, by increasing the plasticizer amount, the T_g decreases. The T_g values of the PLA_ATEC mixtures appear slightly lower with respect to PLA_ATBC mixtures, likely due to a higher interaction density between the PLA chains and the ATEC molecules, which are characterized by lower dimensions of the non-interacting alkyl groups. This could reduce the size of the PLA cooperativity region and accordingly the glass transition temperature [19].

Comparison between the T_g values listed in Table 3 and the T_g data reported in Table 5 for increasing ATEC and ATBC concentration reveals that the concentration of the plasticizers in the MAF of the semi-crystalline PLA_ATEC_5 and PLA_ATBC_5 mixtures is between about 6.5 % and 8.0 %, increasing with crystallinity (see Fig. S4 in the

Table 4
Unit cell parameters, cell volume and crystal density of PLA from XRD analysis of semi-crystalline PLA, PLA_ATEC_5 and PLA_ATBC_5 samples.

Sample	*a* [Å]	*b* [Å]	*c* [Å]	Volume [Å^3]	ρ_C [g/cm^3]
PLA	10.65 ± 0.02	6.02 ± 0.01	28.99 ± 0.05	1858 ± 10	1.287 ± 0.005
PLA_ATEC_5	10.65 ± 0.01	6.03 ± 0.01	29.01 ± 0.03	1862 ± 7	1.284 ± 0.005
PLA_ATBC_5	10.64 ± 0.02	6.03 ± 0.01	29.04 ± 0.05	1863 ± 8	1.284 ± 0.005

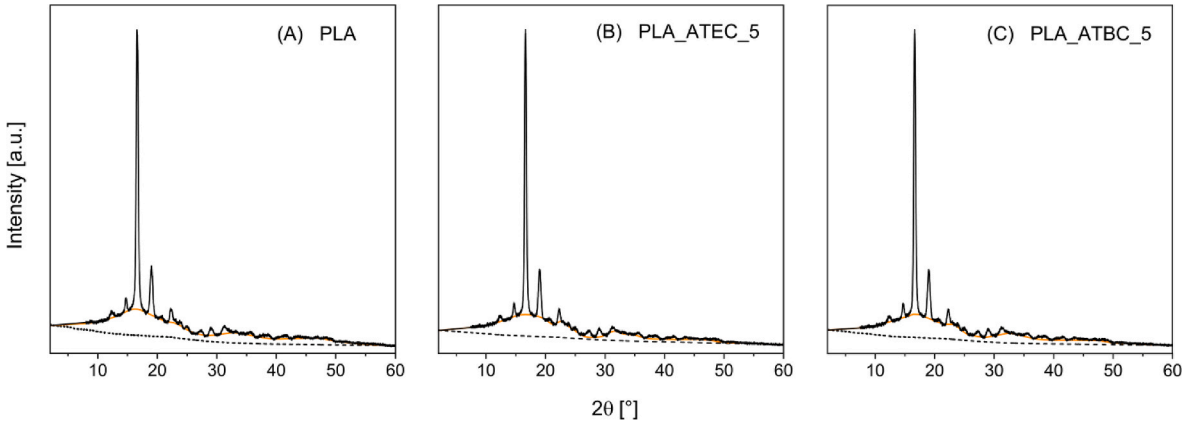

Fig. 3. XRD patterns of (A) PLA, (B) PLA_ATEC_5 and (C) PLA_ATBC_5 at T_{room} after crystallization at T_{mould} = 120 °C for t_{mould} = 20 min. The scattering of the amorphous phase (orange line) is also shown, as well as the background (black dashed line).

Table 5
Glass transition temperatures (T_g); experimental elastic modulus (E); tensile strength at break (TS), elongation at break at T_{room} of amorphous PLA_ATEC and PLA_ATBC mixtures with increasing plasticizer weight fraction. Estimated errors from repeated measurements: ±0.5 K for T_g; ±0.05 GPa for E; ±1 MPa for TS; ±0.2 for the elongation at break.

Sample	T_g [°C]	E [GPa]	TS [MPa]	Elongation at break [%]
PLA_ATEC_5	48.5	3.15	50	4.0
PLA_ATEC_7	46.0	3.06	47	4.1
PLA_ATEC_9	42.0	2.96	41	4.2
PLA_ATBC_5	49.0	3.13	54	3.9
PLA_ATBC_7	46.5	3.08	44	4.0
PLA_ATBC_9	42.5	2.99	43	4.1

Supplementary Data). From these percentage values, the ATEC and ATBC amount in the MAF ($g_{plast\ in\ MAF}$) was calculated (see Table 6, where all values refer to 1 g of mixture.) For example, for t_{mould} = 10 min, a percentage of 6.3 % of ATEC means that the PLA MAF amount is 93.7 %. Being the PLA MAF 0.69 g, it can be deduced that the ATEC mass in the MAF is 0.04_6 g. The ATEC molecules not included in the MAF were clearly embedded in the RAF. Thus, the ATEC amount in the RAF ($g_{plast\ in\ RAF}$) was estimated as difference ($g_{plast\ in\ RAF} = g_{plast} - g_{plast\ in\ MAF}$) and the relative percentage was obtained as: $g_{plast\ in\ RAF}/(g_{plast\ in\ RAF} + g_{RAF,PLA})$. Similarly, the ATEC and ATBC quantities present in the MAF and RAF after different t_{mould}s were derived (see Table 6).

Table 6 shows that the ATEC and ATBC concentration in the MAF increases with the crystallization progress, and it is equal in the PLA_ATEC_5 and PLA_ATBC_5 mixtures. In parallel, the ATEC and ATBC concentration in the RAF decreases. Most likely, the large ATEC and ATBC molecules are progressively rejected from the RAF, due to the stress and constraints imposed by the crystalline segments, which could hinder their accommodation. It was proven that the free volume of PLA increases during crystallization due to the formation of many and smaller holes localized in the RAF [62]. For the holes present in the MAF, an average volume of about 93 Å^3 was estimated [63]. This value is much lower of the van der Waals volume of the ATEC and ATBC molecules, *i.e.* the space impenetrable to other molecules, which, calculated according to a group contribution method [64], is approximately 280 and 380 Å^3, respectively. Thus, by taking into account that the holes in the RAF are generally smaller than those in the MAF [62], it is intuitive to imagine how the large ATEC and ATBC molecules can be hardly embedded between the constrained amorphous segments of the RAF. The progressive decrease of the ATEC and ATBC concentration in the RAF region could be linked to the growth of lamellae in more restricted amorphous areas. The formation of these subsidiary lamellae could require the removal of the plasticizer molecules from the growth front, due to difficult rearrangements provoked by the close already existing lamellae. In any case, the ATBC percentage that remains trapped in the RAF is slightly higher with respect to the smaller sized ATEC, most likely due to its higher dimensions and more complicated migration. The analysis of the Hansen's parameters relative to PLA, ATEC and ATBC (δ = 20.1, 18.9 and 18.0 (J/cm^3)$^{1/2}$ respectively) [22] demonstrates that the intermolecular cohesive forces between PLA and ATEC are higher with respect to those of the PLA/ATBC mixture. This confirms that the lower removal of the ATBC molecules from the RAF is due to hindered migration and not to favoured intermolecular interactions.

Table 6
Estimation of the ATEC and ATBC accumulation in the MAF ($g_{plast\ in\ MAF}$) and RAF ($g_{plast\ in\ RAF}$) of the PLA_ATEC_5 and PLA_ATBC_5 mixtures during crystallization. All the values refer to 1 g of mixture. g_{PLA} and g_{plast} are the weights of PLA and the plasticizer, respectively. The weights of the crystalline, mobile amorphous and rigid amorphous fractions ($g_{C,PLA}$, $g_{MAF,PLA}$ and $g_{RAF,PLA}$) correspond to $w_{C,PLA}$, $w_{MAF,PLA}$ and $w_{RAF,PLA}$, as listed in Table 3.

Sample	g_{PLA} [g]	$g_{C,PLA}$ [g]	$g_{MAF,PLA}$ [g]	$g_{RAF,PLA}$ [g]	g_{plast} [g]	$g_{plast\ in\ MAF}$ [g]	$g_{plast\ in\ RAF}$ [g]
PLA_ATEC_5 t_{mould} = 10 min	0.95	0.19	0.69	0.07	0.05	0.04_6 (6.3 %)	0.00_4 (5.4 %)
PLA_ATEC_5 t_{mould} = 14 min	0.95	0.28	0.58	0.09	0.05	0.04_5 (7.2 %)	0.00_5 (5.2 %)
PLA_ATEC_5 t_{mould} = 20 min	0.95	0.29	0.56	0.10	0.05	0.04_7 (7.8 %)	0.00_3 (3.0 %)
PLA_ATBC_5 t_{mould} = 10 min	0.95	0.24	0.66	0.05	0.05	0.04_4 (6.3 %)	0.00_6 (10.7 %)
PLA_ATBC_5 t_{mould} = 14 min	0.95	0.30	0.55	0.10	0.05	0.04_3 (7.2 %)	0.00_7 (6.5 %)
PLA_ATBC_5 t_{mould} = 20 min	0.95	0.31	0.50	0.14	0.05	0.04_2 (7.8 %)	0.00_8 (5.4 %)

3.4. Tensile characterization of amorphous and semi-crystalline pure and plasticized PLA samples

The values of the experimental elastic modulus (E), tensile strength at break (TS), and elongation at break measured at T_{room} for amorphous and semi-crystalline samples after crystallization at T_{mould} = 120 °C for different moulding times, are listed in Table 3. The tensile properties of the analysed samples differ due to the crystallinity increase with the moulding time. The higher the sample residence time, the greater the brittleness, which results in an elastic modulus increment and in a decrement of both the stress and elongation at break. The fracture behaviour of all the semicrystalline specimens appears brittle, supporting the idea of crystalline domains considered as stress concentrators leading to premature failure of the materials. The addition of the plasticizes induces a small decrease in the elastic modulus and tensile strength, whereas the elongation at break increases, in agreement with literature data [23].

To better correlate the mechanical properties of PLA, PLA_ATEC_5 and PLA_ATBC_5 samples with phase composition, from the crystalline weight fraction, and the mobile amorphous and rigid amorphous weight fractions including both PLA and the plasticizer ($g_{MAF,PLA}$+$g_{plast\ in\ MAF}$ and $g_{RAF,PLA}$+$g_{plast\ in\ RAF}$, respectively, see Table 6), the corresponding volume fractions (v_C, v_{MAF} and v_{RAF}) were estimated. As densities of the crystal phase (ρ_C) and the mobile amorphous fraction (ρ_{MAF}), 1.285 g/cm^3 and 1.25 g/cm^3 [60,61] were utilized, respectively. By assuming the density of the RAF (i) equal to that of the MAF, or (ii) slightly lower (approximately – 10 %, according to previous estimations performed for PLLA and other polymers [42,62,65,66]) almost identical v_C, v_{MAF} and v_{RAF} values were obtained (±0.01). The calculated volume fractions, v_C, v_{MAF} and v_{RAF}, listed in Tables 7 and 8 for PLA, PLA_ATEC_5 and PLA_ATBC_5, are however almost equivalent to the respective crystalline, mobile amorphous and rigid amorphous weight fractions.

3.5. Modelling of the tensile elastic modulus of the RAF of semi-crystalline pure and plasticized PLA

For the estimation of the elastic modulus of the RAF in pure and plasticized PLA, the two- and three-phase models previously applied to pure semi-crystalline PLLA were adopted as a first attempt [42]. The schematic representation of these two- and three-phase Takayanagi

Table 7
Crystalline (v_C), mobile amorphous (v_{MAF}) and rigid amorphous (v_{RAF}) volume fractions of PLA, PLA_ATEC_5 and PLA_ATBC_5 samples; texture parameters (λ and φ) and elastic modulus of the crystal phase and the connected RAF (E_C'), calculated according to the SP_2 phase model; texture parameters (α and β), elastic modulus of the crystal phase (E_C) and elastic modulus of the rigid amorphous fraction (E_{RAF}), calculated according to the SP_3 phase model.

Sample	v_C	v_{MAF}	v_{RAF}	λ (Eq. (3))	φ (Eq. (3))	E_C' [GPa] (Eq. (3))	α (Eq. (4))	β (Eq. (4))	E_C [GPa] (Eq. (4))	E_{RAF} [GPa] (Eq. (4))
PLA t_{mould} = 6 min	0.16	0.73	0.11	0.14	0.42	13.0	0.40	0.53	13.2	5.8
PLA t_{mould} = 10 min	0.30	0.54	0.16	0.27	0.65	13.5	0.56	0.33	14.6	5.9
PLA t_{mould} = 20 min	0.31	0.50	0.19	0.30	0.66	13.5	0.57	0.32	14.6	5.9
PLA_ATEC_5 t_{mould} = 10 min	0.19	0.74	0.07	0.17	0.47	13.2	0.41	0.52	14.2	5.8
PLA_ATEC_5 t_{mould} = 14 min	0.27	0.63	0.10	0.29	0.66	13.8	0.57	0.32	14.8	5.8
PLA_ATEC_5 t_{mould} = 20 min	0.28	0.62	0.10	0.32	0.67	13.8	0.58	0.30	14.9	5.9
PLA_ATBC_5 t_{mould} = 10 min	0.23	0.71	0.06	0.20	0.50	13.3	0.42	0.51	14.7	5.8
PLA_ATBC_5 t_{mould} = 14 min	0.29	0.60	0.11	0.29	0.66	13.7	0.56	0.33	15.0	5.8
PLA_ATBC_5 t_{mould} = 20 min	0.30	0.55	0.15	0.32	0.67	13.9	0.59	0.30	15.0	5.9

Table 8
Crystalline (v_C), mobile amorphous (v_{MAF}) and rigid amorphous (v_{RAF}) volume fractions of the PLA, PLA_ATEC_5 and PLA_ATBC_5 samples; texture parameters (λ and φ) and elastic modulus of the crystal phase and the connected RAF (E_C') (calculated according to the PS_2 phase model), texture parameters (α and β), elastic modulus of the crystal phase (E_C) and elastic modulus of the rigid amorphous fraction (E_{RAF}) (calculated according to the PS_3 phase model).

Sample	v_C	v_{MAF}	v_{RAF}	λ (Eq. (5))	φ (Eq. (5))	E_C' [GPa] (Eq. (5))	α (Eq. (6))	β (Eq. (6))	E_C [GPa] (Eq. (6))	E_{RAF} [GPa] (Eq. (6))
PLA t_{mould} = 6 min	0.16	0.73	0.11	0.19	0.40	11.7	0.34	0.57	13.9	4.7
PLA t_{mould} = 10 min	0.30	0.54	0.16	0.27	0.61	12.6	0.52	0.34	14.3	5.1
PLA t_{mould} = 20 min	0.31	0.50	0.19	0.28	0.62	12.7	0.53	0.32	14.0	5.3
PLA_ATEC_5 t_{mould} = 10 min	0.19	0.74	0.07	0.23	0.52	12.1	0.49	0.49	13.9	5.1
PLA_ATEC_5 t_{mould} = 14 min	0.27	0.63	0.10	0.29	0.66	12.9	0.60	0.32	14.3	5.3
PLA_ATEC_5 t_{mould} = 20 min	0.28	0.62	0.10	0.30	0.68	13.2	0.61	0.30	14.3	5.5
PLA_ATBC_5 t_{mould} = 10 min	0.23	0.71	0.06	0.25	0.59	12.5	0.56	0.42	14.1	5.1
PLA_ATBC_5 t_{mould} = 14 min	0.29	0.60	0.11	0.28	0.65	13.0	0.58	0.33	14.0	5.6
PLA_ATBC_5 t_{mould} = 20 min	0.30	0.55	0.15	0.29	0.66	12.9	0.59	0.31	13.9	5.5

models, which consist of series-parallel arrangements (SP_2 phase and SP_3 phase, respectively), is shown in Fig. 4. These models represent a situation with crystalline domains dispersed in the amorphous phase, as it takes place in semi-crystalline polymers with low or intermediate crystallinity degree. As experimental findings and theoretical estimations suggested that the elastic modulus of the RAF is higher than that of the MAF [36–39], in the two-phase model the crystal phase and the RAF were considered as a single block, due to the tight connection between these two fractions. Conversely, in the three-phase model, the RAF was inserted as separate block between the MAF and the crystal. The texture parameters λ, φ, α and β, which range from 0 to 1, are connected to the phase composition and the degree of parallel and series coupling of the different phases. Thus, in the model SP_2 phase, the product λφ is connected to the sum of the volume fractions of the crystal phase and the RAF, whereas (1-λφ) is linked to the volume fraction of the MAF. For the model SP_3 phase, the volume fraction of the crystal phase is linked to the product λα, the volume fraction of the MAF to (1-λ+βλ), and the volume fraction of the RAF to λ(1-α-β).

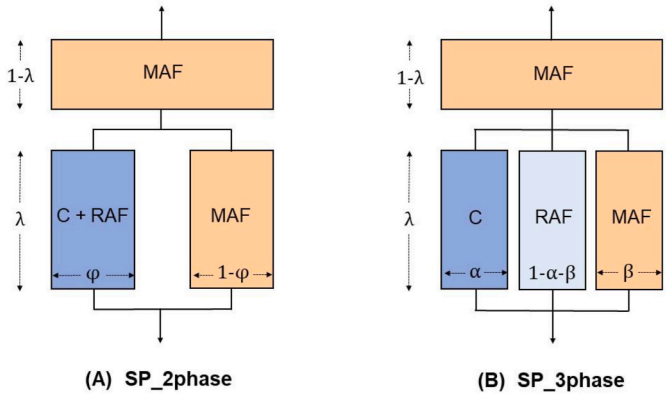

Fig. 4. Schematic representation of (A) the 2-phase (SP_2 phase) and (B) the 3-phase (SP_3 phase) mechanical models of semi-crystalline polymers according to the series-parallel arrangement of the crystalline (C), mobile amorphous (MAF) and rigid amorphous (RAF) fractions. In these models, the crystalline lamellae are parallel to the stress direction.

The equations that express the elastic modulus of semi-crystalline polymers according to the SP_2 phase and SP_3 phase models are respectively:

$$\frac{1}{E}=\frac{1-\lambda}{E_{MAF}}+\frac{\lambda}{\varphi E_C{}'+(1-\varphi)E_{MAF}} \tag{3}$$

$$\frac{1}{E}=\frac{1-\lambda}{E_{MAF}}+\frac{\lambda}{\alpha E_C+(1-\alpha-\beta)E_{RAF}+\beta E_{MAF}} \tag{4}$$

where E is the elastic modulus of the semi-crystalline polymer, E_C' the overall elastic modulus of the crystal phase and the connected RAF, E_C the elastic modulus of the crystal phase, E_{MAF} the elastic modulus of the mobile amorphous fraction and E_{RAF} the elastic modulus of the rigid amorphous fraction. This theoretical approach considers E_C', E_C and E_{RAF} as unknown quantities, whereas the experimental values of E_{MAF} are maintained fixed. The analysis was applied to pure PLA and the plasticized PLA samples. A two-step procedure was utilized. First, an iterative numerical method (by means of Excel Data Solver Function) was utilized to calculate the parameters λ, φ and E_C' according to the SP_2 phase model, by minimization of the error between the experimental and the theoretical elastic moduli predicted by Eq. (3). The calculated λ parameters were successively maintained fixed for the resolution of Eq. (4), to estimate the parameters α, β, E_C and E_{RAF}, on the basis of the SP_3 phase model. The experimental and theoretical value reported in the literature for the crystalline elastic modulus of PLLA α-form, E_C = 14 GPa [67] was utilized as initial value for E_C' (first iteration) and E_C (second iteration), whereas initial values between 4 and 8 GPa were assumed for E_{RAF} (second iterations). The combinations of parameters producing the smallest deviation between the experimental and calculated elastic modulus were chosen as final results. For E_{MAF}, the following fixed values were utilized: 3.3 GPa for pure PLA (see Table 3), 3.1 GPa for PLA_ATEC_5 and PLA_ATEC_5, corresponding to a plasticizer amount of about 7 wt% (see Table 5).

Table 7 lists the calculated λ, φ and E_C' values, linked to the mechanical configuration SP_2 phase (Eq. (3)), followed by the α, β, E_C and E_{RAF} values connected to the mechanical configuration SP_3 phase (Eq. (4)). For comparison with the calculated texture parameters, Table 7 also displays the volumetric crystalline, mobile amorphous and rigid amorphous fractions (v_C, v_{MAF}, and v_{RAF}, respectively).

Inspection of Table 7 shows that the product λφ correctly increases like the sum of the volumetric fractions (v_C + v_{RAF}). The E_C' values calculated by Eq. (3) appear close to the theoretical value for the crystalline elastic modulus of PLLA α-form, which is around 14 GPa [67], although E_C' also includes the RAF modulus. The resolution of Eq. (4) for the SP_3 phase model leads to E_C data slightly higher than the theoretical value, together with a proper trend of the texture parameters α and β: λα and λ(1-α-β) correctly increase like v_C and v_{RAF}, whereas (1-λ+ βλ) decreases like v_{MAF}. The calculated E_{RAF} values are very similar to the value previously estimated for PLLA by utilizing the same SP_3 phase method [42]. A E_{RAF} value included between E_C and E_{MAF} is in perfect agreement with intuitive and theoretical expectations: weaker intermolecular interactions with respect to the crystal phase validate a lower E_{RAF} value with respect to E_C, whereas a higher chain rigidity with respect to the MAF rationalizes a higher E_{RAF} value with respect to E_{MAF}. No difference between the E_{RAF} values for pure and plasticized PLA was estimated.

With the aim of modelling the systems under study as correctly as possible, an additional attempt was performed by considering that pure PLA and plasticized PLA samples were prepared by injection-moulding at high injection pressure. Operative conditions of injection-moulding have important effects on the crystal morphology. Three distinct crystalline zones have been reported in the cross-section of specimens prepared by injection-moulding [68]: a skin layer with fibrillar morphology, containing highly oriented lamellar structures, a shear zone with crystallinity orientation that progressively decreases as the distance from the skin increases, and a core zone with spherulitic morphology with no preferred orientation. For PLA it was also found that injection-moulding produces non-spherulitic semi-crystalline structures in the skin region, due to the strong orientation of the melt, so that the growth of short lamellae perpendicular to the flow direction was detected [69]. Although the tensile elastic modulus of PLLA α-crystals exhibits marked isotropy, with a theoretical modulus along the chain axis only slightly higher than that in the perpendicular direction [67], it could be useful to consider a different arrangement of the phases. Indeed, by switching from an iso-strain condition for the linked crystalline, mobile amorphous and rigid amorphous fractions, as in the SP_3 phase model, to an iso-stress condition, it is possible to take into account the presence of oriented crystals. Fig. 5 shows parallel-series arrangements (PS_2 phase and the PS_3 phase), in which the crystalline lamellae are perpendicular to the stress direction.

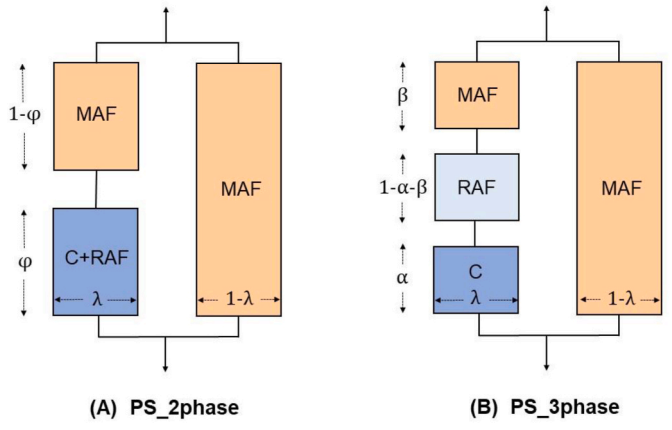

Fig. 5. Schematic representation of (A) the 2-phase (PS_2 phase) and (B) the 3-phase (PS_3 phase) mechanical models of semi-crystalline polymers according to the parallel-series arrangement of the crystalline (C), mobile amorphous (MAF) and rigid amorphous (RAF) fractions. In these models, the crystalline lamellae are perpendicular to the stress direction.

The equations that describe the elastic modulus according to configurations PS_2 phase and the PS_3 phase are respectively:

$$E = (1-\lambda)E_{MAF} + \frac{\lambda E_C E_{MAF}}{\varphi E_{MAF} + (1-\varphi)E_C'} \quad (5)$$

$$E = (1-\lambda)E_{MAF} + \frac{\lambda E_C E_{MAF} E_{RAF}}{\alpha E_{MAF} E_{RAF} + \beta E_C E_{RAF} + (1-\alpha-\beta)E_C E_{MAF}} \quad (6)$$

The same two-step procedure described above was again applied, and the results are collected in Table 8. For the PS_2 phase model, the product λφ correctly increases like the sum ($v_C + v_{RAF}$), as well as, for the PS_3 phase model, λα and λ(1-α-β), which increase like v_C and v_{RAF}, whereas (1-λ+ βλ) decreases like v_{MAF}. The most important results are that, by utilizing these parallel-series arrangements, E_C' correctly turns out lower that the theoretical crystalline elastic modulus of PLLA α-form (14 GPa), whereas E_C values perfectly match with it. The E_{RAF} values for the PLA_ATEC_5 and PLA_ATBC_5 mixtures do not substantially differ from that of pure PLA, which means that ATEC and ATBC do not act as plasticizers in the RAF region, due to the stronger constraints exerted by the close crystals. This analysis proves that the parallel-series arrangement is the most accurate description of injection-moulded specimens with partial crystals alignment.

Experimental confirmation of the morphological arrangement of the amorphous fractions in pure and plasticized PLA could be provided by Atomic Force Microscopy (AFM) analysis [70], which could also allow the measurement of the elastic modulus of the amorphous phase as a function of the distance from the crystals. This route will be possibly investigated in a successive study.

4. Conclusions

The main focus of the present study has been the investigation of the ATEC and ATBC distribution in the MAF and RAF regions of PLA/ATEC and PLA/ATBC mixtures containing 5 wt% of plasticizer. Accurate measurements of the specific heat capacity of pure and plasticized PLA proved that the addition of ATEC and ATBC to PLA does not lead to the development of strong specific interactions between the two components, as the interactions that are established are likely similar to those active in pure PLA.

An estimation of the ATEC and ATBC concentration in the MAF and RAF of the PLA_ATEC_5 and PLA_ATBC_5 mixtures during crystallization displayed that the plasticizer percentage progressively increases in the MAF up to about 8 wt%, whereas it decreases in the RAF region. The progressive decrease of the plasticizer concentration in the rigid amorphous interphase could be linked to the growth of subsidiary lamellae. The formation of these secondary lamellae in more restricted areas could request the removal of the plasticizer molecules from the growth front. The ATBC concentration in the RAF was estimated higher with respect to the ATEC concentration, likely due to its greater steric hindrance and slower migration.

The present study also proposes an estimation of the tensile elastic modulus of the RAF connected to α-crystals in semi-crystalline PLA, PLA_ATEC_5 and PLA_ATBC_5. The calculations were performed on the basis of mechanical analytical models widely applied to semi-crystalline polymers, here modified according to a three-phase approach. To identify the mechanical model that better represents the morphological organization in PLA samples prepared by injection-moulding at high injection pressure, two different models were considered, with crystalline lamellae parallel and perpendicular to the stress direction, respectively. The most appropriate model turned out to be the parallel-series arrangement, with crystalline lamellae perpendicular to the stress direction, in agreement with the presence of oriented lamellar structures in the specimens. The mathematical procedure led to an E_C value for the α-phase in excellent agreement with the theoretical value reported in the

literature ($E_C = 14$ GPa), and to a E_{RAF} value around 5.5 GPa for pure and plasticized PLA. This means that the ATEC and ATBC molecules do not exert plasticizing action on the RAF, whose mobility is mainly governed by the close crystal regions.

CRediT authorship contribution statement

Giovanna Molinari: Data curation, Formal analysis, Investigation, Writing – review & editing. **Laura Aliotta:** Data curation, Writing – review & editing. **Mauro Gemmi:** Funding acquisition, Validation, Writing – review & editing. **Andrea Lazzeri:** Conceptualization, Funding acquisition, Validation, Writing – review & editing. **Maria Cristina Righetti:** Conceptualization, Data curation, Formal analysis, Investigation, Methodology, Supervision, Validation, Writing – original draft, Writing – review & editing.

Declaration of competing interest

The authors declare that they have no known competing financial interests or personal relationships that could have appeared to influence the work reported in this paper.

Data availability

Data will be made available on request.

Appendix A. Supplementary data

Supplementary data to this article can be found online at https://doi.org/10.1016/j.polymertesting.2024.108325.

References

[1] A.P. Gupta, V. Kumar, New emerging trends in synthetic biodegradable polymers – polylactide: a critique, Eur. Polym. J. 43 (2007) 4053–4074, https://doi.org/10.1016/j.eurpolymj.2007.06.045.

[2] L.T. Lim, R. Auras, M. Rubino, Processing technologies for poly(lactic acid), Prog. Polym. Sci. 33 (2008) 820–852, https://doi.org/10.1016/j.progpolymsci.2008.05.004.

[3] S. Saeidlou, M.A. Huneault, H. Li, C.B. Park, Poly(lactic acid) crystallization, Prog. Polym. Sci. 37 (2012) 1657–1677, https://doi.org/10.1016/j.progpolymsci.2012.07.005.

[4] P. Pan, Y. Inoue, Polymorphism and isomorphism in biodegradable polyesters, Prog. Polym. Sci. 34 (2009) 605–640, https://doi.org/10.1016/j.progpolymsci.2009.01.003.

[5] R. Androsch, C. Schick, M.L. Di Lorenzo, Melting of conformationally disordered crystals α'-phase of poly(L-lactic acid), Macromol. Chem. Phys. 215 (2014) 1134–1139, https://doi.org/10.1002/macp.201400126.

[6] T. Kawai, N. Rahman, G. Matsuba, K. Nishida, T. Kanaya, M. Nakano, H. Okamoto, J. Kawada, A. Usuki, N. Honma, K. Nakajima, M. Matsuda, Crystallization and melting behavior of poly(l-lactic acid), Macromolecules 40 (2007) 9463–9469, https://doi.org/10.1021/ma070082c.

[7] J. Zhang, K. Tashiro, H. Tsuji, A.J. Domb, Disorder-to-Order phase transition and Multiple melting behavior of poly(L-lactide) investigated by simultaneous measurements of WAXD and DSC, Macromolecules 41 (2008) 1352–1357, https://doi.org/10.1021/ma0706071.

[8] R. Androsch, M.L. Di Lorenzo, C. Schick, Crystal nucleation in random L/D-lactide copolymers, Eur. Polym. J. 75 (2016) 474–485, https://doi.org/10.1016/j.eurpolymj.2016.01.020.

[9] P. Song, L. Sang, C. Jin, Z. Wei, Temperature-dependent polymorphic crystallization of pol(l-lactide)s on the basis of optical purity and microstructure, Polymer 134 (2018) 163–174, https://doi.org/10.1016/j.polymer.2017.11.069.

[10] E. Blázquez-Blázquez, R. Barranco-García, T.M. Díez-Rodríguez, M.L. Cerrada, E. Pérez, Combined effects from dual incorporation of ATBC as plasticizer and mesoporous MCM-41 as nucleating agent on the PLA isothermal crystallization in environmentally-friendly ternary composite systems, Polymers 15 (2023) 624, https://doi.org/10.3390/polym15030624.

[11] K.S. Anderson, K.M. Schreck, M.A. Hillmyer, Toughening polylactide, Polym. Rev. 48 (2008) 85–108, https://doi.org/10.1080/15583720701834216.

[12] H. Liu, J. Zhang, Research progress in toughening modification of poly(lactic acid), J. Polym. Sci., Polym. Phys. Ed. 49 (2011) 1051–1083, https://doi.org/10.1002/polb.22283.

[13] G. Kfoury, J.-M. Raquez, F. Hassouna, J. Odent, V. Toniazzo, D. Ruch, P. Dubois, Recent advances in high performance poly(lactide): from "green" plasticization to super-tough materials via- (reactive) compounding, Front. Chem. 1 (2013) 32, https://doi.org/10.3389/fchem.2013.00032.

[14] X.-R. Gao, Y. Li, H.-D. Huang, J.-Z. Xu, L. Xu, X. Ji, G.-J. Zhong, Z.-M. Li, Extensional stress-induced orientation and crystallization can regulate the balance of toughness and stiffness of polylactide films: interplay of oriented amorphous chains and crystallites, Macromolecules 52 (2019) 5278–5288, https://doi.org/10.1021/acs.macromol.9b00932.

[15] X. Zhao, H. Hu, X. Wang, X. Yu, W. Zhou, S. Peng, Super tough poly(lactic acid) blends: a comprehensive review, RSC Adv. 10 (2020) 13316, https://doi.org/10.1039/D0RA01801E.

[16] S. Coiai, M.L. Di Lorenzo, P. Cinelli, M.C. Righetti, E. Passaglia, Binary Green Blends of Poly(lactic acid) with Poly(butylene adipate-co-butylene terephthalate) and Poly(butylene succinate-co-butylene adipate) and Their Nanocomposites, Polymers 13 (2021) 2489, https://doi.org/10.3390/polym13152489.

[17] M.L. Di Lorenzo, Poly(L-Lactic acid)/poly(butylene succinate) biobased biodegradable blends, Polym. Rev. 61 (2021) 457–492, https://doi.org/10.1080/15583724.2020.1850475.

[18] I. Fortelny, A. Ujcic, L. Fambri, M. Slouf, Phase structure, compatibility, and toughness of PLA/PCL blends: a review, Front. Mater. 6 (2019) 206, https://doi.org/10.3389/fmats.2019.00206.

[19] L. Dobircau, N. Delpouve, R. Herbinet, S. Domenek, L. Le Pluart, L. Delbreilh, V. Ducruet, E. Dargent, Molecular mobility and physical ageing of plasticized poly(lactide), Polym. Eng. Sci. 55 (2015) 858–865, https://doi.org/10.1002/pen.23952.

[20] A. Marcilla, M. Beltran, Mechanism of plasticizers action, in: G. Wypych (Ed.), Handbook of Plasticizers, fourth ed., ChemTec Publishing, Toronto, 2023, pp. 139–158.

[21] L.V. Labrecque, R.A. Kumar, V. Davè, R.A. Gross, S.P. McCarthy, Citrate esters as plasticizers for poly (lactic acid), J. Appl. Polym. Sci. 66 (1997) 1507–1513, https://doi.org/10.1002/(SICI)1097-4628(19971121)66:8<1507::AID-APP11>3.0.CO;2-0.

[22] N. Ljungberg, B. Wesslen, The effects of plasticizers on the dynamic mechanical and thermal properties of poly(lactic acid), J. Appl. Polym. Sci. 86 (2002) 1227–1234, https://doi.org/10.1002/app.11077.

[23] M. Baiardo, G. Frisoni, M. Scandola, M. Rimelen, D. Lips, D. Ruffieux, E. Wintermantel, Thermal and mechanical properties of plasticized poly(L-lactic acid), J. Appl. Polym. Sci. 90 (2003) 1731–1738, https://doi.org/10.1002/app.12549.

[24] H. Li, M.A. Huneault, Effect of nucleation and plasticization on the crystallization of poly(lactic acid), Polymer 48 (2007) 6855–6866, https://doi.org/10.1016/j.polymer.2007.09.020.

[25] C. Courgneau, S. Domenek, A. Guinault, L. Averous, V. Ducruet, Analysis of the structure-properties relationships of different multiphase systems based on plasticized poly(lactic acid), J. Polym. Environ. 19 (2011) 362–371, https://doi.org/10.1007/s10924-011-0285-5.

[26] V. Arias, A. Hoglund, K. Odelius, A.-C. Albertsson, Polylactides with "green" plasticizers: influence of isomer composition, J. Appl. Polym. Sci. 130 (2013) 2962–2970, https://doi.org/10.1002/app.39446.

[27] M. Safandowska, A. Rozanski, Ring-banded spherulites in polylactide and its blends, Polym. Test. 100 (2021) 107230, https://doi.org/10.1016/j.polymertesting.2021.107230.

[28] S. Araujo, N. Delpouve, S. Domenek, A. Guinault, R. Golovchak, R. Szatanik, A. Ingram, C. Fauchard, L. Delbreilh, E. Dargent, Cooperativity scaling and free volume in plasticized polylactide, Macromolecules 52 (2019) 6107–6115, https://doi.org/10.1021/acs.macromol.9b00464.

[29] E. Quero, A.J. Müller, F. Signori, M.-B. Coltelli, S. Bronco, Isothermal cold-crystallization of PLA/PBAT blends with and without the addition of acetyl tributyl citrate, Macromol. Chem. Phys. 213 (2012) 36–48, https://doi.org/10.1002/macp.201100437.

[30] Z. Kulinski, E. Piorkowska, Crystallization, structure and properties of plasticized poly(L-lactide), Polymer 46 (2005) 10290–10300, https://doi.org/10.1016/j.polymer.2005.07.101.

[31] E. Piorkowska, Z. Kulinski, A. Galeski, R. Masirek, Plasticization of semicrystalline poly(l-lactide) with poly(propylene glycol), Polymer 47 (2006) 7178–7188, https://doi.org/10.1016/j.polymer.2006.03.115.

[32] B. Wunderlich, Reversible crystallization and the rigid amorphous phase in semicrystalline macromolecules, Prog. Polym. Sci. 28 (2003) 383–450, https://doi.org/10.1016/S0079-6700(02)00085-0.

[33] M.C. Righetti, D. Prevosto, E. Tombari, Time and temperature evolution of the rigid amorphous fraction and differently constrained amorphous fractions in PLLA, Macromol. Chem. Phys. 217 (2016) 2013–2026, https://doi.org/10.1002/macp.201600210.

[34] M.C. Righetti, Amorphous fractions of poly(lactic acid), Adv. Polym. Sci. 279 (2018) 195–234, https://doi.org/10.1007/12_2016_14.

[35] N. Wang, X. Zhang, X. Ma, J. Fang, Influence of carbon black on the properties of plasticized poly(lactic acid) composites, Polym. Degrad. Stabil. 93 (2008) 1044–1052, https://doi.org/10.1016/j.polymdegradstab.2008.03.023.

[36] R. Rastogi, W.P. Vellinga, S. Rastogi, C. Schick, H.E.H. Meijer, The three-phase structure and mechanical properties of poly(ethylene terephthalate), J. Polym. Sci., Polym. Phys. Ed. 42 (2004) 2092–2106, https://doi.org/10.1002/polb.20096.

[37] M.L. Di Lorenzo, M.C. Righetti, The three-phase structure of isotactic poly(1-butene), Polymer 49 (2008) 1323–1331, https://doi.org/10.1016/j.polymer.2008.01.026.

[38] P.J. in 't Veld, M. Hütter, G.C. Rutledge, Temperature-dependent thermal and elastic properties of the interlamellar phase of semicrystalline polyethylene by molecular simulation, Macromolecules 39 (2006) 439–447, https://doi.org/10.1021/ma0518961.

[39] A. Sedighiamiri, T.B. Van Erp, G.W.M. Peters, L.E. Govaert, J.A.W. Van Dommelen, Micromechanical modeling of the elastic properties of semicrystalline polymers: a three-phase approach, J. Polym. Sci., Polym. Phys. Ed. 48 (2010) 2173–2184, https://doi.org/10.1002/polb.22099.
[40] M. Takayanagi, S. Uemura, S. Minami, Application of equivalent model method to dynamic rheo-optical properties of crystalline polymer, J. Polym. Sci., Polym. Symp. 5 (1964) 113–122, https://doi.org/10.1002/polc.5070050111.
[41] M.C. Righetti, L. Aliotta, N. Mallegni, M. Gazzano, E. Passaglia, P. Cinelli, A. Lazzeri, Constrained amorphous interphase and mechanical properties of poly (3-hydroxybutyrateco- 3-hydroxyvalerate), Front. Chem. 7 (2019) 790, https://doi.org/10.3389/fchem.2019.00790.
[42] L. Aliotta, M. Gazzano, A. Lazzeri, M.C. Righetti, Constrained amorphous interphase in poly(L-lactic acid): estimation of the tensile elastic modulus, ACS Omega 5 (2020) 20890–20902, https://doi.org/10.1021/acsomega.0c02330.
[43] J. Odent, J.-M. Raquez, C. Samuel, S. Barrau, A. Enotiadis, P. Dubois, E. P. Giannelis, Shape-memory behavior of polylactide/silica ionic hybrids, Macromolecules 50 (2017) 2896–2905, https://doi.org/10.1021/acs.macromol.7b00195.
[44] S.M. Sarge, W. Hemminger, E. Gmelin, G. Höhne, H. Cammenga, W. Eysel, Metrologically based procedures for the temperature, heat and heat flow rate calibration of DSC, J. Therm. Anal. 49 (1997) 1125–1134, https://doi.org/10.1007/BF01996802.
[45] A. Wurm, M. Merzlyakov, C. Schick, Reversible melting probed by temperature modulated dynamic mechanical and calorimetric measurements, Colloid Polym. Sci. 276 (1998) 289–296, https://doi.org/10.1007/s003960050242.
[46] R. Androsch, I. Moon, S. Kreitmeier, B. Wunderlich, Determination of heat capacity with a Sawtooth−Type, power compensated temperature modulated DSC, Thermochim. Acta 357–358 (2000) 267–278, https://doi.org/10.1016/S0040-6031(00)00397-X.
[47] M.L. Di Lorenzo, B. Wunderlich, Temperature-modulated calorimetry of the crystallization of polymers analysed by measurements and model, J. Therm. Anal. Calorim. 57 (1999) 459–472, https://doi.org/10.1023/A:1010163923965.
[48] M. Pyda, B. Wunderlich, Reversing and non-reversing heat capacity of poly(lactic acid) in the glass transition region by TMDSC, Macromolecules 38 (2005) 10472–10479, https://doi.org/10.1021/ma051611k.
[49] N. Varol, N. Delpouve, S. Araujo, S. Domenek, A. Guinault, R. Golovchak, A. Ingram, L. Delbreilh, E. Dargent, Amorphous rigidification and cooperativity drop in semi-crystalline plasticized polylactide, Polymer 194 (2020) 122373, https://doi.org/10.1016/j.polymer.2020.122373.
[50] R.S. Barnum, S.H. Goh, J.W. Barlow, D.R. Paul, Excess heat capacities for two miscible polymer blend systems, J. Polym. Sci. Polym. Lett. 23 (1985) 395–401, https://doi.org/10.1002/pol.1985.130230801.
[51] C. Shen, Y. Wang, M. Li, D. Hu, Crystal modifications and multiple melting behavior of poly(L-lactic acid-co-d-Lactic acid), J. Polym. Sci., Polym. Phys. Ed. 49 (2011) 409–413, https://doi.org/10.1002/polb.22175.
[52] M.C. Righetti, M.L. Di Lorenzo, E. Tombari, M. Angiuli, The low-temperature endotherm in poly(ethylene terephthalate):partial melting and rigid amorphous fraction mobilization, J. Phys. Chem. B 112 (2008) 4233–4241, https://doi.org/10.1021/jp076399w.
[53] C. Schick, Temperature modulated differential scanning calorimetry (TMDSC)-Basics and applications to polymers, in: S.Z.D. Cheng (Ed.), Handbook of Thermal Analysis and Calorimetry, Elsevier Science B.V., Amsterdam, 2002, pp. 713–810.
[54] B. Wunderlich, Thermal Analysis of Polymeric Materials, Springer-Verlag, Berlin, 2005, p. 689.
[55] M. Yasuniwa, K. Sakamo, Y. Ono, W. Kawahara, Melting behavior of poly(l-lactic acid): X-ray and DSC analyses of the melting process, Polymer 49 (2008) 1943–1951, https://doi.org/10.1016/j.polymer.2008.02.034.
[56] M.C. Righetti, M. Gazzano, M.L. Di Lorenzo, R. Androsch, Enthalpy of melting of α′- and α-crystals of poly(L-lactic acid), Eur. Polym. J. 70 (2015) 215–220, https://doi.org/10.1016/j.eurpolymj.2015.07.024.
[57] M. Safandowka, C. Makarewicz, A. Rozanski, R. Idczak, Barrier properties of semicrystalline polylactide: the role of the density of the amorphous regions, Macromolecules 55 (2022) 10077–10089, https://doi.org/10.1021/acs.macromol.2c01490.
[58] M.F.C. Ladd, R.A. Palmer, Structure Determination by X-Ray Crystallography, second ed., Plenum Press, New York, 1985, p. 65.
[59] B. Lotz, Crystal polymorphism and morphologyof polylactides, Adv. Polym. Sci. 279 (2018) 273–302, https://doi.org/10.1007/12_2016_15.
[60] E.W. Fisher, H.J. Sterzel, G. Wegner, Investigation of the structure of solution grown crystals of lactide copolymers by means of chemical reactions, Kolloid-Z. u. Z. Polymere 251 (1973) 980–990, https://doi.org/10.1007/BF01498927.
[61] D. Sawai, Y. Tsugane, M. Tamada, T. Kanamoto, M. Sungil, S.H. Hyon, Crystal density and heat of fusion for a stereo-complex of poly(L-lactic acid) and poly(D-lactic acid, J. Polym. Sci., Polym. Phys. Ed. 45 (2007) 2632–2639, https://doi.org/10.1002/polb.21270.
[62] J. del Río, A. Etxeberria, N. López-Rodríguez, E. Lizundia, J.R. Sarasua, A PALS contribution to the supramolecular structure of poly(L-lactide), Macromolecules 43 (2010) 4698–4707, https://doi.org/10.1021/ma902247y.
[63] X. Zhao, J. Li, X. Yu, S. Yang, J. Liu, W. Zhou, S. Peng, Microstructure and barrier properties of reactive compatibilized PLA/PA11 blends investigated by positron annihilation lifetime spectroscopy, Polym. Test. 115 (2022) 107763, https://doi.org/10.1016/j.polymertesting.2022.107763.
[64] D.W. van Krevelen, K. te Nijenhuis, Properties of Polymers, fourth ed., Elsevier B. V., Amsterdam, 2009, pp. 71–108.
[65] J. Lin, S. Shenogin, S. Nazarenko, Oxygen solubility and specific volume of rigid amorphous fraction in semicrystalline poly(ethylene terephthalate), Polymer 43 (2002) 4733–4743, https://doi.org/10.1016/S0032-3861(02)00278-1.
[66] M.C. Righetti, M. Vannini, A. Celli, D. Cangialosi, C. Marega, Bio-based semi-crystalline PEF: temperature dependence of the constrained amorphous interphase and amorphous chain mobility in relation to crystallization, Polymer 247 (2022) 124771, https://doi.org/10.1016/j.polymer.2022.124771.
[67] K. Wasanasuk, K. Tashiro, Theoretical and experimental evaluation of crystallite moduli of various crystalline forms of poly(L-lactic acid), Macromolecules 45 (2012) 7019–7026, https://doi.org/10.1021/ma3010982.
[68] R. Pantani, I. Coccorullo, V. Speranza, G. Titomanlio, Modeling of morphology evolution in the injection molding process of thermoplastic polymers, Prog. Polym. Sci. 30 (2005) 1185–1222, https://doi.org/10.1016/j.progpolymsci.2005.09.001.
[69] M. Du, K. Jariyavidyanont, R. Boldt, M. Tariq, M. Fischer, Y. Spoerer, I. Kuehnert, R. Androsch, Crystal-nuclei formation during injection-molding of poly (L-lactic acid), Polymer 250 (2022) 124897, https://doi.org/10.1016/j.polymer.2022.124897.
[70] M. Zhang, Y. Li, P.V. Kolluru, L.C. Brinson, Determination of mechanical properties of polymer interphase using combined atomic force microscope (AFM) experiments and finite element simulations, Macromolecules 51 (2018) 8229–8240, https://doi.org/10.1021/acs.macromol.8b01427.